Velocities and sizes of outgoing droplets after impact on a wall heated above the Leidenfrost temperature

P. Dunand[1,2], G. Castanet[1,2*], P. Villedieu[3], O. Caballina[1,2], F. Lemoine[1,2]
1: Université de Lorraine, LEMTA, UMR 7563, France
2: CNRS, LEMTA, UMR 7563, France
3: ONERA, Toulouse, France

Abstract

In a wide variety of applications, interactions between sprays and hot walls remain difficult to integrate due to poor understanding of the flow and heat transfer characteristics. In the present study, the emphasis is placed on the impact of droplets onto a wall heated above the Leidenfrost temperature. Shadow imaging using a high-speed (HS) camera allows visualizing the droplet impacts. An innovative drop sizing method combined with Particle Tracking Velocimetry, is implemented. The method offers benefits of measuring droplet of irregular shape while providing directly their spatial distribution. Tracking of the particle results in a lagrangian description of the flow, particularly valuable for the modeling of the impacts. The main results of the image processing concern droplet velocities and sizes before and after the impact, as well as the maximum spreading diameter and the residence time in the case of a droplet rebound. Experiments are undertaken in order to improve and validate droplet-wall interaction models.

Introduction

The interactions between sprays and hot walls occur in a wide variety of industrial applications, for example, the development of compact high pressure direct injection engines. In this situation, impaction of fuel droplets onto cylinder walls affects noticeably the combustion efficiency and the emissions of pollutants. Another application is related to the cooling of hot surfaces in the metal processing industry. Spray cooling is widely used due to its high efficiency, low coolant consumption and the possibility to achieve a relative spatially homogeneous heat transfer [1, 2]. When the wall temperature is sufficiently high, a vapour layer is immediately formed between the wall and the droplet, which prevents the direct contact between the liquid and the solid. This regime, generally called Leidenfrost regime or film boiling regime, is characterized by poor heat transfer rates between the liquid and solid. Hydrodynamic also plays an important role. It is mainly controlled by the Weber number (*We*). For $We<30$, droplets spread and rebound. When $30<We<80$, the droplets spread similarly as in the previous case, but separate into a few number of satellite droplets after leaving the wall during their rebound. For $We>80$, disintegration occurs in the initial spreading stage. This last regime is generally called splashing.

Wachters and Westerling (1966)[3] pioneered the study of heat transfer and hydrodynamic of droplets in the film boiling regime. They determined experimentally a relationship between the Weber number of the droplets before and after the impact in the case of a rebound. These authors assumed a preservation of the tangential component of the velocity. Watkins and Wang [4], Parks and Watkins [5] introduced a coefficient taking into account the normal and tangential to the wall loss of momentum. Karl and Frohn [6] did a comprehensive study of the rebound of water and ethanol droplets. They developed correlations for the loss of momentum and the maximum spreading diameter, however their measurements were restricted to $We<30$.

The splashing was also of interests in many studies. Among others, Naber and Farrel [7], Parks and Watkins [5] or Bai and Gosman [8] provided the number of droplets resulting from the break-up of a single drop impacting on a hot surface as a linear function of the Weber number. Akhtar and Yule [9] investigated the impact of quasi-monodisperse droplets onto a polished heated steel target, for a very large Weber number range (100-750). Combining high-speed shadowgraphy and PDA allow these authors extracting a wide range of data such as the sauter mean diameter of the secondary droplets and established empirical correlation as a function of the Weber number. Richter et al. [10], considered the impingement of a droplet chain made of isooctane droplets (around 90 µm in diameter). They used shadowgraphy and PIV to investigate the effect of the wall temperature and incident Weber number on the Sauter Mean Diameters (SMD) and velocities of the secondary droplets. The emphasis was put also on the influence of the impingement frequency on the secondary droplet formation. The study of the impact of multiple droplet chains by Müller et al. [11]also reveals an important influence of spatial interactions on the SMD. Moita and Moreira [12] proposed a more refined investigation of the splashing. These authors provided a very detailed description of the disintegration mechanism. The Sauter mean diameter of the secondary droplets (SMD) was found to depend on both Reynolds and Weber number.

* Corresponding author: guillaume.castanet@univ-lorraine.fr

The aim of the present study is to develop and validate models for the droplets/wall interactions in the film boiling regime. To that end, an innovative measurement method based on high-speed shadowgraphy, is developed in order to characterize the main parameters of interest, i.e. the size and velocity distributions of the primary and secondary droplets as well as the spreading diameter and residence time in the case of a rebound.

Experimental setup

The experimental setup is presented in figure 1. It has already been described by Dunand et al. [13] who investigated the heat transfer associated with spray cooling in the film boiling regime. A piezoelectric injector is used to produce a chain of mono-sized and equally spaced droplets. The droplets range from 80 µm to 250 µm, while their velocity is set to a few m/s. Droplets collide with a thin slice of nickel heated by induction beyond the Leidenfrost temperature. The droplet generator can be rotated to modify the direction of the droplet stream and hence the normal velocity of the droplets and the impact regime. The upper surface of the nickel on which the droplet are impacting, is polished so as to obtain a very smooth surface. A high-speed (HS) camera (Phantom v710, Vision Research) is used to visualize the drop impacts. It can provide up to 7,500 fps at full resolution (1,280 x 800 pixels, 20 µm pixel size). A zoom lens (OPTEM zoom 125C minimized configuration) allows observing with a magnification ranging from 2.1 to 26. Given the small aperture of the zoom, it is required to illuminate the droplets from behind using a very bright light source (a 400W HMI lamp with a parabolic reflector) in order to obtain contrasted shadow images with a short exposure time (set here at 1 µs). Time-resolved visualizations of the droplet impacts require having acquisition rates close to 80,000 fps at a reduced resolution in terms of pixels (in comparison the injection frequency of the droplet is on the order of 10000 Hz). Figures 2 and 3 shows typical examples of rebound and splashing obtained with this optical configuration.

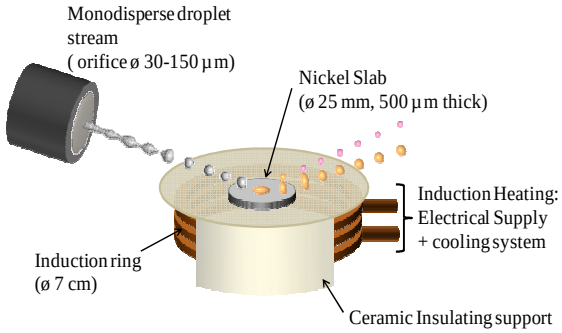

Figure 1 Experimental setup

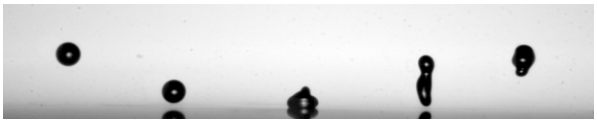

Figure 2 Rebound of water droplets (D_d=138 µm, We_n=15.25, V_n=2.82 m/s, V=8.34 m/s, f_{inj}=11 000 Hz)

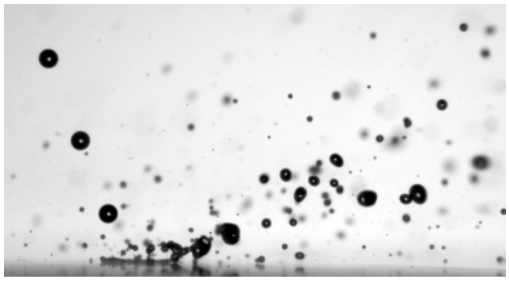

Figure 3 Splashing of water droplets (D_d= 118 µm We_n= 107.4, V=8.645 m/s, f_{inj}= 16 400 Hz))

Size and velocity measurements

For the purpose of the study, a digital image analysis technique has been developed to characterize droplet sizes and velocities in the context of spray cooling. Recently, Richter et al. [10] and Murray et al. [14] reported the use of shadow imagery to study droplet splashing. In this study, shadow imagery was combined to PIV to obtain the eulerian velocity field of the droplets as well as their size distributions. However, size and velocity measurements were disconnected. In this study, a high-camera allows visualizing the droplet impacts by means of a shadow imaging system. Image processing is divided in two distinct steps: identification of droplets and the tracking of their trajectories.

a) Identification of droplets and size measurements

Image pre-processing - The processing begins with a normalization of the images. This stage aims at obtaining a uniform background in the image given that the light source can be non homogenous. The normalization corresponds to a division of the images by a background image (obtained without any object). The images are also corrected from the barrel distortion using a grid of dots periodically spaced.

Detection of the droplet outlines - Detecting the smallest droplets is of prime importance given their large occurrence. Segmentation methods based on predefined values of gray level or gradient thresholds are not adapted to this situation since it is extremely difficult to find a suitable threshold value regardless of the droplet size. Difficulties are also related to the presence of blurred droplets that can modify locally the background

around the in-focused droplets. In this study, these considerations led to take the steepest slope as an indicator of the droplet outlines. Particle detection consists in searching the zeros in the image's laplacian L and the zones where it is positive (since the laplacian becomes positive in the interior of the particles). To limit the noise, a Gaussian filter is applied before calculating the laplacian. This filtering is moderate in order not to enlarge the droplets and make the smallest droplets disappear. As some ripples remains in L and can lead to the detection of false particles, a threshold L_1 is applied. Valid particles are defined as being positive regions of L where at least one pixel verifies $L>L_1>0$. L_1 is set to slightly exceed the height of the ripples. Closed lines corresponding to $L=0$, are interpreted as the edge of the droplets. Their interpolation allows having subpixel contour extraction.

Separation of overlapped particles - The previously described detection method allows separating most of the droplets when they are partially overlapping from the very beginning of their identification. If a separation is applied, it is mainly for the particle tracking since missing particles can be difficult to handle. Two strategies are used in parallel. The grey-level image is seen as a topographic relief and the watershed transform allows finding valleys, which are of interest for separation. A second method examines the curvature of their outlines and identifies pairs of points that correspond to a narrowing of the contour.

Computation of droplet parameters – The diameter D of a droplet is based on the area A inside the sub-pixel contour. Assuming a circular shape, D is given by $\sqrt{A/\pi}$. The centroid of the particle is calculated from all points of the area A inside the contour. It is interpreted as the center of mass of the particle for its tracking. Depth of field (DOF) can potentially introduce biases in the size measurements. The gray-level gradient at the particle boundaries and the maximum gray-level intensity inside the particle are computed as they have been suggested as a relevant indicator for the DOF [15-17] [17, 18].

b) Tracking of the particles trajectories

PTV was chosen from scratch over PIV since droplets can have very different displacements within an interrogation window, particularly near the breakup zone at the wall collision. Moreover, PIV allow obtaining the eulerian velocity field of the droplets, while a tracking of the particle trajectory would result in a lagrangian description of the flow, particularly valuable for the modeling of the impact process. In turn, this approach enables to correct the bias of the size distribution toward the slowest droplets. Without tracking, the slowest droplets that appear in more images than the fastest ones are counted more times. The algorithm is based on a Multiple Hypothesis Tracking (MHT) method. This kind of approach can be easily adapted to the case of droplet splashing. It is a preferred technique for solving the data association problem in modern multiple targets tracking systems in cluttered environment [19, 20]. The approach consists in generating a set of data-association hypothesis to account for all possible origins of every measurement (here the positions of the centroids of the detected particles). In practical, the method relies on building all the possible associations between tracks and measurements for a number of successive frames and comparing them. All the hypothetical associations can be represented as a tree, whose branches correspond to a potential track. Algorithm is divided in several stages: initiation of tracks, track formation and extension, track termination, clustering and selection of the potential tracks. The basic idea is that an object must not belong to several tracks at the same time. A selection is thus applied so as to retain only the tracks that are the more probable (tracks having the most regular trajectory and a sufficient number of elements.

c) Droplet classification

The sign of the velocity is used to sort the droplets into classes. Tracks with an initial velocity directed upward are classified as secondary droplets. A heuristic-based approach allows distinguishing the primary droplets from the ternary droplets (secondary droplets coming back to the wall with a downward velocity). An illustration of the classification is given in figure 9. In the case of a bouncing (with or without formation of satellite droplets), it is possible to connect every primary droplets to all the secondary droplets it has created. In the case of a splashing, droplets in contact with the wall are excluded from the tracking and no relationship is sought between primary and secondary droplets.

Measurement accuracy and tracking performances

A plate dotted with discs of different size is used to assess the accuracy of the size measurements and to characterize the effect of the DOF. Discs range from 4 μm to 500 μm, which covers the whole droplet sizes encountered in the experiments (figure 4). The same parameters are utilized for the detection of the patterns as in the study of the droplet/wall interactions.

a) Size measurement accuracy

Figure 5 presents the measurement errors as a function of the disc sizes when the plate is at the focal plane of the camera. A systematic error of about 4 µm can be observed for droplets larger than 40 µm. This corresponds to less than 1/2 pixel. For the smallest droplets, the overestimation of the sizes is more important. Subpixel interpolation of contours seems less accurate for very small objects. The fitted red curve is used to correct these errors. Furthermore, by changing the brightness of the lamp, it was possible to evaluate the sensibility of the objects size measurements to the background level. It has been verified that this sensibility is very weak.

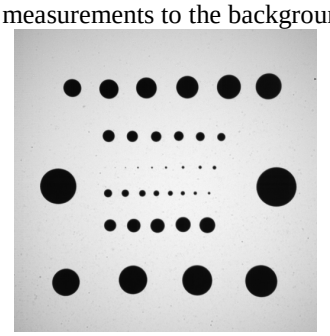

Figure 4 Calibration plate dotted with discs ranging from 4 µm to 0.5 mm.

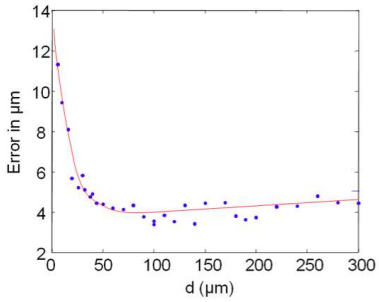

Figure 5 Errors in size measurement as a function of the disc diameters.

b) Out-of-focus droplets and measurement volume

The plate is moved back and forth along the optical axis. As expected, the DOF (the maximum distance over which the droplet can be detected and identified) increases with the size of the object (figure 6). Figure 7 shows the measurements error as a function of the distance z to the focal plane. Errors are moderate in an interval of z=+/- 0.5 mm, which corresponds to the region where most of the droplets are located in the experiments.

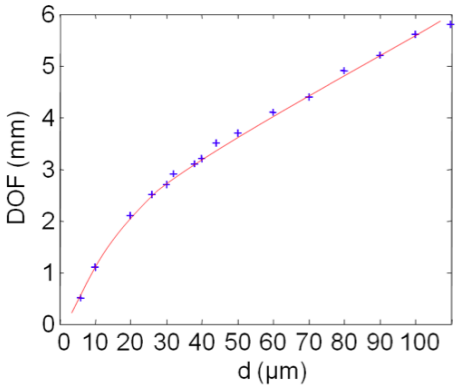

Figure 6 DOF vs. sizes of the discs

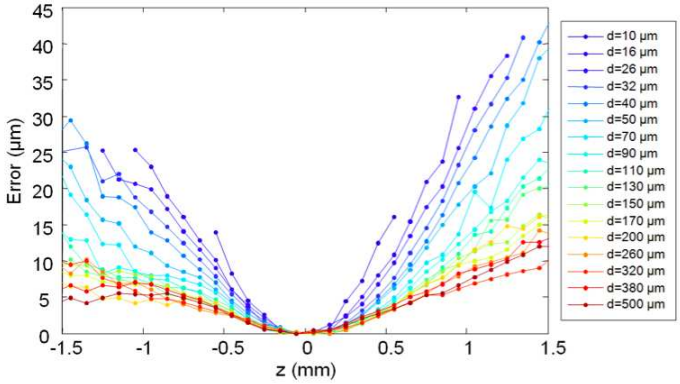

Figure 7 Size measurement errors as a function of the distance to the focal plane z.

A droplet size is attributed to each track (lagrangian approach). It corresponds to the size of the element that is the most focused. An in-focus criterion is required to eliminate tracks that are located outside of a considered measurement volume. A measurement volume limited to z=+/-1.5 mm was chosen as it is relevant in terms of mass flux conservation (i.e. few droplets are eliminated in practice). The gradient at the droplet edge was found to be more relevant for the largest droplets than the maximum level intensity in the contour. Gradient was used thus, since large droplets are the only ones to be detected outside the selected measurement volume (figure 6).

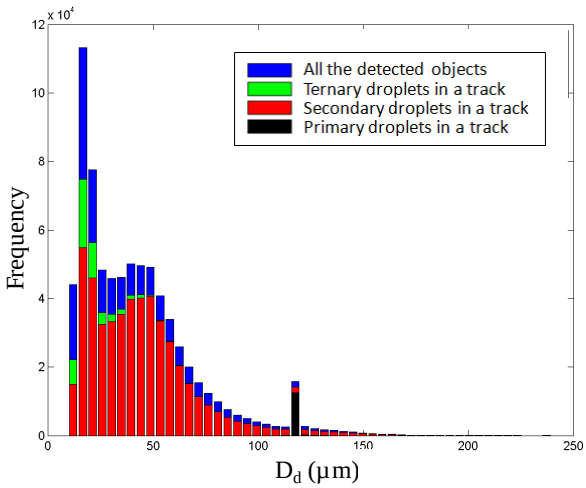

Figure 8 Size distributions of the droplets included in a track (case of the splashing in figure 3)

c) Tracking performances

In order to estimate the performances of the tracking method, the rejection rate (percentage of objects not included in a track) has been calculated. This rate is less than 1% in the case of a rebound and it is about 20-25% in the case of a splashing. The size distribution of the objects included in a track is similar to that of all the objects that have been detected (figure 8). This suggests that the tracking is only slightly biased by the

size of the droplets. Additionally, the volume flow rate of the secondary droplets crossing a closed frontier was found to be comparable to that of the primary droplets.

Results and discussion

A comprehensive set of experiments was performed to investigate the effects of dimensionless numbers such as Weber and Reynolds numbers. Two liquids were tested: water and ethanol.

a) Bouncing regime

Loss of momentum- An important parameter for the description of the rebounds is the loss of momentum. Normal and tangential components of the velocity of the primary droplets ($v_{n,1}$,$v_{t,1}$) and the secondary droplets ($v_{n,2}$,$v_{t,2}$) have been extracted from the measurements. Figure 9 and 16 shows the evolutions of the restitution coefficients $r_n = v_{n,2}/v_{n,1}$ and $r_t = v_{t,2}/v_{t,1}$ as a function of the normal Weber $We_n = \rho V_{n,1}^2 d/\gamma$. For We_n>30, rebounds with satellites droplets are usually observed. The velocity taken for the calculation of the momentum is the (volume) velocity weighed by the liquid volume defined by:

$$v_d = \sum_i v_i \, d_i^3 \Big/ \sum_i d_i^3 \,, \qquad (1)$$

where i denotes the i^{th} secondary droplets (validated track). As expected, both velocity ratios r_n and r_t decrease with We_n. The experiments reveal that the loss of momentum tangential to the wall, $\left(m v_{d1,t} - m v_{d2,t}\right)/m v_{d1,t} = 1 - r_t$, m being the initial droplet mass, is less important than the loss of momentum normal to the wall (1-r_n). Contrary to a general statement, the loss of momentum tangential to the wall is not negligible in the bouncing regime since it can reach 20% in the case of water. In practice, it is significant when We_n>30. The measurements were compared to existing empirical models. Park and Watkins [5] proposed a correlation for the tangential and normal coefficients of restitution based on the angle α between the inlet velocity and the normal to the wall (θ would be the angle between the inlet velocity and the wall). They claimed the tangential and normal coefficients of restitution to be equal, which is not observed in figures 9 and 10. However, their correlation fits relatively well the values of r_t (figure 10). Correlation established by Karl and Frohn [6] for We_n<30 is in good agreement with the measurements of r_n (figure 10). Results are also comparable to that of Wachters and Westerling [3]. None of the tested models account for the liquid viscosity, while the loss of momentum is mainly caused by internal dissipation due to viscous forces during the droplet deformation process. One would expect an influence of the Ohnesorge number *Oh* or the Reynolds number *Re*. Differences between water and ethanol may be attributed to a dependence on the Ohnesorge number, (*Oh* is about 3 times higher for ethanol than for water), but more investigation seems necessary to conclude.

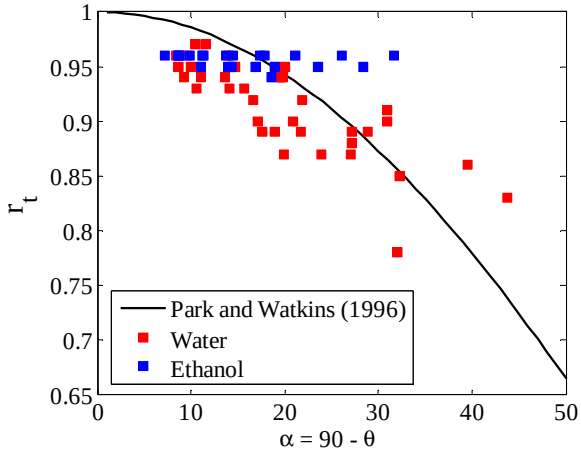

Figure 9 Coefficient of restitution of the tangential velocity vs. the incident angle

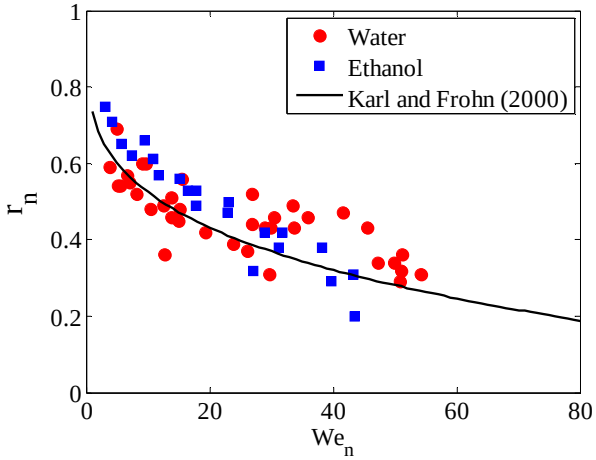

Figure 10 Coefficient of restitution of the normal velocity vs. the normal Weber number

Maximum spreading diameter- During their interaction with the wall, droplets expand radially. This spreading process is stopped by surface tension. Existing models for the maximum spreading diameter are based on the conservation of mechanical energy. Kinetic energy is transformed into surface energy and it is generally admitted that all the kinetic energy is converted into surface energy at the maximum deformation. However, an unknown part of energy has been dissipated. Karl and Frohn [6] assumed that the droplets take a cylindrical shape during their deformation. They also considered that half the loss of momentum (figure 11) has to be taken into account in the energy balance as dissipation when the droplet reaches its maximum radial expansion. No clear justification is given for this amount of dissipated energy. As for the loss of momentum, measurements of the maximum spreading diameter are in agreement with Karl and Frohn [6]. The present results seem to indicate that their approach is not limited to We_n<30 but it can be extended to higher values of We_n.

Residence time- The residence time correspond to the time from the initial instant of contact with the surface to the instant of departure. It is usually expressed as the first-order vibration period t_{res} of a freely oscillating droplet:

$$t_{res} = \pi/4\sqrt{\rho d^3/\gamma} \tag{2}$$

Dividing by $d/v_{1,n}$, a dimensionless expression for t_{res} is obtained:

$$t^*_{res} = \frac{t_{res}\, v_{1,n}}{d} = \frac{\pi}{4}\sqrt{We_n} \tag{3}$$

In presence of dissipation, the droplet can be considered as a damped harmonic oscillator as deformation remains moderated (i.e. low values of We_n). In that case, the droplet oscillates with a slightly different frequency than the undamped case:

$$t^*_{res} = C\sqrt{We_n} \text{ with } C = \frac{\pi}{4}\Big/\sqrt{1-\varsigma^2}\,, \tag{4}$$

where $\varsigma < 1$ is the damping factor related to the dissipation. Measured values of t^*_{res} were fitted by a power law:

$$t^*_{res} = \alpha We_n^{\beta} \text{ with } \alpha = 1.095 \text{ and } \beta = 0.415 \tag{5}$$

Figure 12 shows that $\beta = 0.5$ is acceptable for We_n<30 but it can lead to a significant overestimate of the residence time at higher We_n. For We_n>30, the assumption of a linear (deformation) behavior is certainly less valid. The time t_{max} from the instant of contact to the instant of maximum spreading is also of interest. Its variation with We_n is plotted in figure 13 and interpolation of the data leads to:

$$t^*_{\max} = \alpha We_n^{\beta} \text{ with } \alpha = 0.378 \text{ and } \beta = 0.337 \tag{6}$$

For We_n>20, it appears in figure 12 that $t^*_{\max} \approx 1/4\, t^*_{res}$,while $t^*_{\max}$ tends to about 1/3 as We_n becomes very small.

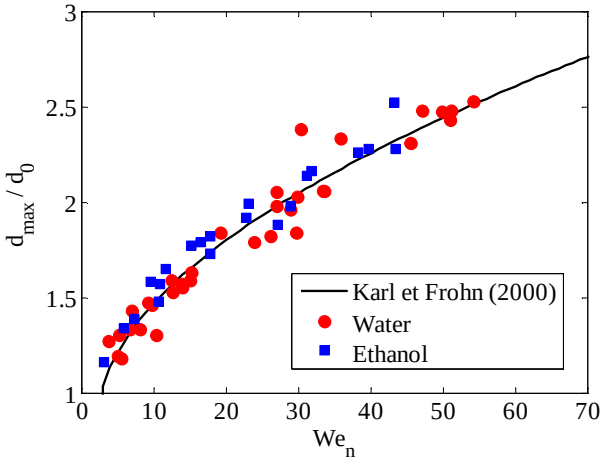

Figure 11 Normalized maximum spreading diameter as a function of the normal Weber number We_n

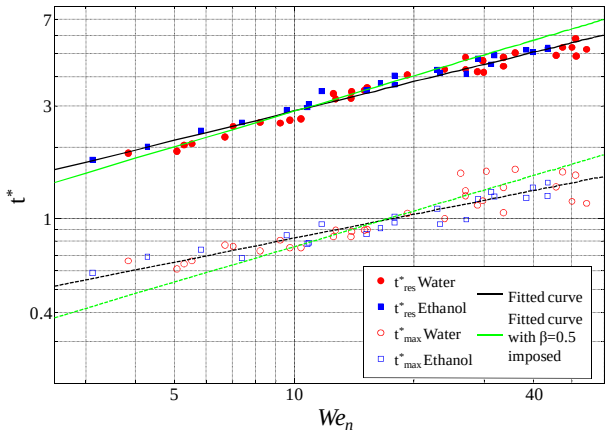

Figure 12 Normalized residence time and maximum spreading time as a function of We_n

b) Splashing regime

Measurements of the Sauter diameter d_{32} have been compared to existing models. To the best of our knowledge, there is no correlation to predict the shape and extend of the droplet size distribution. In some cases, the size distribution can be bimodal (figure 8). Images suggest that some of the smallest droplets could be generated by the boiling in the liquid film in addition to the film breakup. Different mechanisms of droplet reatomization can thus play a role. In the film boiling regime, the size of the secondary droplets is dependent on the Weber number, as noticed by Akhtar and Yule [9]. Yarin and Weiss [21] suggested a dependence on the Reynolds number. Han et al. [22] considered a combination of both these dimensionless numbers. Moita and Moreira [12] investigated impaction of quite large droplets (around 2 mm in diameter) on a heated target, for liquids having different surface tensions and viscosities and Weber numbers ranging from 24 to 1117. They suggested that the Sauter Mean Diameter d_{32} can be written as:

$$d_{32}/d_0 = A We_n^{\,a}\, \mathrm{Re}^b \text{ with } A = 52.77,\ a = -0.6 \text{ and } b = -0.23. \tag{7}$$

In this expression, the negative exponents mean that droplets with larger viscosity and/or surface tension generate larger secondary droplets. As presented in figure 13, measurements obtained in this study are in a good agreement with equation(7). In this figure, triangles correspond to the cases where a coalescence of the incoming droplets has been observed (figure 14). Coalescence occurs because of the high frequency of the droplet impaction, on the order of 20 kHz. Consecutive droplets are merging during the spreading of their liquid films. This phenomenon may lead to an increase in the Sauter diameter as it can be seen in figure 14.

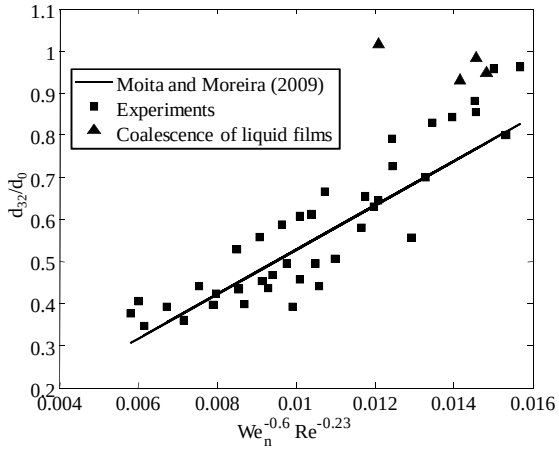

Figure 13 Evolution of the normalized Sauter mean diameter ; illustration of equation (7)

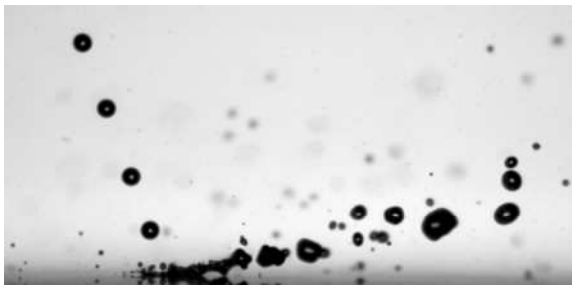

Figure 14 Example of liquid film coalescence during the spreading of consecutive droplets (f_{inj}= 24500 Hz, d_0= 103.18 µm, We_n= 108, V_n= 8.69 m/s)

Velocities of the secondary droplets- The volume averaged velocity v_d defined in equation (1) has been used to study the global loss of momentum during the splashing of water droplets.

Figure 15 shows the reduction in normal and tangential components of the velocity as a function of the normal Weber number. In this figure, data associated to the bouncing regime are also plotted. This highlights that coefficients r_n and r_t have an almost continuous behaviour during the transition between the bouncing and the splashing regimes. The loss of tangential momentum increases with We_n in the splashing regime, while the loss of normal momentum seems to reach an asymptotic value. Park and Watkins [5] suggested that the normal velocity component of the secondary droplets can be obtained by using the Weber number corresponding to the tail of the Wachters and Westerling curve in [3], which features the Weber number after impact versus the Weber number before impact. Results from Wachters and Westerling [3] reveal that the normal Weber number after the impact is close to 1 for We_n>80.

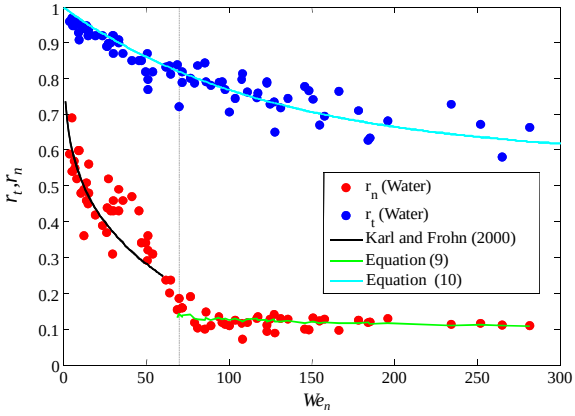

Figure 15 Reduction of the normal and tangential component of the droplet velocities as a function of the normal Weber number.

This immediately gives the following expression for the normal component of the velocity:

$$v_{n,2} = \sqrt{\gamma/\rho d_2}\ , \tag{8}$$

where subscript 2 stands for secondary droplet. Using equation (7) coming from the study of Moita and Moreira [12] for the diameter of the secondary droplets, the normal restitution coefficient can be expressed by :

$$r_n = A_2\, We_n^{\,a2}\, \mathrm{Re}^{b2}\,, \text{with } a_2 = -0.5(a+1) = -0.2\,,\ b_2 = -0.5b = 0.46 \text{ and } A_2 = A^{-0.5} = 26.385 \tag{9}$$

For the tangential component of the velocity, experimental results for water can be fitted by:

$$r_t = 1 + 0.58\left(1 - \exp\left(-0.008\,We_n\right)\right) \text{ for } We_n < 300 \tag{10}$$

Conclusions and perspectives

An innovative drop sizing method combined with Particle Tracking Velocimetry, based on high-speed shadowgraphy, was implemented to investigate droplet impact onto a heated wall in the film-boiling regime. The main results obtained from image processing concern the droplet velocities and sizes before and after the impact, the maximum spreading diameter as well as the droplet residence time. An extensive comparison was performed with the models existing in the literature and some of them were extended.

The restitution coefficient, i.e. the ratio between the velocities after and before the impact appear continuous, regardless the regime of impact (bouncing or splashing). Contrary to the available literature, the restitution coefficient of tangential velocity is decreasing with the Weber number. The restitution coefficient for the normal velocity was found to decrease continuously in the rebound regime, as it attains quickly an asymptotic value, predicted by Park and Watkins [5], in the splashing regime, when the correlation of Moita and Moreira [12] for the Sauter Mean Diameter was used. The maximum spreading diameter was found to be in

good agreement with the model provided by Karl and Frohn [6], and a new expression was proposed for the residence time as a power law of the Weber number which slightly differs from the usually used expressions in $We_n^{1/2}$, due to the viscous dissipation. The Sauter Mean Diameter of secondary droplets was found to depend on a combination of both normal Weber number and Reynolds number, in good agreement with the results of Moita and Moreira [12], but on a much larger field of validity.
Further investigations will concern the detailed investigation of the distribution functions of the size and velocity components of the secondary droplets in the splashing regime. In parallel, the heat flux removed from the heated wall was estimated by combining infrared thermography on the rear face of the wall and a semi-analytic inverse conduction model. The resulting cooling efficiency will be analyzed in the light of the relevant parameters.

References

[1] J. D. Bernardin and I. Mudawar, *International Journal of Heat and Mass Transfer* 40: 2579-2593 (1997).
[2] J. Kim, *International Journal of Heat and Fluid Flow* 28: 753-767 (2007).
[3] L. H. J. Wachters and N. A. J. Westerling, *Chemical Engineering Science* 21: 1047-1056 (1966).
[4] A. P. Watkins and D. M. Wang, *Proc. Comodia,* 243-248, (1990).
[5] K. Park and A. P. Watkins, *International Journal of Heat and Fluid Flow* 17: 424-438 (1996).
[6] A. Karl and A. Frohn, *Physics of Fluids* 12: 785-796 (2000).
[7] J. D. Naber and P. Farrel, *SAE Tech Paper (*1993).
[8] C. X. Bai and A. D. Gosman, *SAE Tech Paper (*1995).
[9] S. W. Akhtar and A. J. Yule, *ILASS Conference Proceedings Zurich,* 2-6 September 2001.
[10] B. Richter, K. Dullenkopf, and H. J. Bauer, *Experiments in Fluids* 39: 351-363 (2005).
[11] A. Müller, E. Velios, K. Dullenkopf, and H. J. Bauer, *Proceedings of the 11th Triennal International Conference on Liquid Atomization and Spray Systems, Vail, Colorado, USA,* 2009.
[12] A. Moita and A. Moreira, *Experiments in Fluids* 47: 755-768 (2009).
[13] P. Dunand, G. Castanet, and F. Lemoine, *Experiments in Fluids 52(4): 843-856* (2012).
[14] A. Müller, K. Dullenkopf, and H.-J. Bauer, *14th Int Symp on Applications of Laser Techniques to Fluid Mechanics*, Lisbon, Portugal, 2008.
[15] A. Lecuona, P. A. Sosa, P. A. Rodriguez, and R. I. Zequeira, *Measurement Science and Technology* 11, (2000).
[16] E. Fantini, L. Tognotti, and A. Tonazzini, *Computers and Chemical Engineering* 14: 1201-1211 (1990).
[17] K. U. Koh, J. Y. Kim, and S. Y. Lee, *Atomization and Sprays* 9: 313-329 (1999).
[18] H. Malot and J.-B. Blaisot, *Particle & Particle Systems Characterization* 17: 146-158 (2000).
[19] N. Chenouard, I. Bloch, and J.-C. Olivo-Marin, *International Conference on Image Processing,* Cairo, Egypt, 2009.
[20] D. B. Reid, *IEEE Trans. on Automatic Control* AC: 843-854 (1979).
[21] A. L. Yarin and D. A. Weiss, *Journal of Fluid Mechanics* 283: 141-173 (1995).
[22] Z. Han, Z. Xu, and N. Trigui, *Int. J. Engine. Res* 1: 127-146 (2000).